metals

MDPI

Article

Effects of In Situ TiB_2 on the Microstructural Evolution, Mechanical Properties, and Friction Behavior of the Al-Si-Cu Alloys Processed by Laser Powder-Bed Fusion

Zhongxue He [1], Jianying Wang [1], Mengzhen Zhu [1], Tao Wen [1], Feipeng Yang [1], Shouxun Ji [2], Jianming Zheng [3], Ling Shan [3] and Hailin Yang [1,*]

[1] State Key Laboratory of Powder Metallurgy, Central South University, Changsha 410083, China; 223312084@csu.edu.cn (Z.H.); jianying.wang@csu.edu.cn (J.W.); 223301014@csu.edu.cn (M.Z.); 213301068@csu.edu.cn (T.W.); yangfp@csu.edu.cn (F.Y.)

[2] Brunel Centre for Advanced Solidification Technology (BCAST), Brunel University London, Uxbridge UB8 3PH, UK; shouxun.ji@brunel.ac.uk

[3] Zhejiang Wanfeng Precision Casting Co., Ltd., Shaoxing 312400, China; jianming.zheng@wfjyjt.con (J.Z.); ling.shan@wfjyjt.con (L.S.)

* Correspondence: y-hailin@csu.edu.cn

Abstract: In the present study, the densification behavior, microstructural evolution, mechanical properties, and friction behavior of a TiB_2/Al8SiCu composite and Al8SiCu alloy manufactured by laser powder-bed fusion (PBF-LB) were systematically investigated. The results confirm that the addition of in situ TiB_2 particles into Al8SiCu alloys reduce the volumetric energy density required for a high-density TiB_2/Al8SiCu composite. The TiB_2 particles promoted a transformation of columnar to equiaxed crystals and the formation of high-angle grain boundaries. The grains on the vertical direction of the PBF-LBed TiB_2/Al8SiCu composite were much finer than those of the PBF-LBed Al8SiCu alloy. The addition of TiB_2 promoted the grain refinement of the Al8SiCu alloy, of which the average grain size decreased from 15.31 μm to 7.34 μm. The yield strength (YS), ultimate tensile strength (UTS), and elongation (El) of the PBF-LBed Al8SiCu alloy were 296 ± 6 MPa, 517 ± 6 MPa, and 11.7 ± 1.0%, respectively. The PBF-LBed TiB_2/Al8SiCu composite achieved a balance between strength and ductility with a yield strength of 328 ± 8 MPa, an ultimate tensile strength of 541 ± 3 MPa, and an elongation of 9.1 ± 0.7%. The increase in strength mainly resulted from grain boundary strengthening, dislocation strengthening, load-bearing strengthening, solid-solution strengthening, and Orowan strengthening, of which the dislocation strengthening and Orowan strengthening were critical. The enhanced hardness associated with the grain refinement and the formation of the in situ TiB_2 particles also led to an enhanced tribological performance, of which reductions in the average friction coefficient from 0.655 to 0.580 and wear rate from 1.76×10^{-3} mm^3/Nm to 1.38×10^{-3} mm^3/Nm were found.

Keywords: aluminum matrix composites; microstructure; mechanical properties; laser powder-bed fusion; wear behavior

Citation: He, Z.; Wang, J.; Zhu, M.; Wen, T.; Yang, F.; Ji, S.; Zheng, J.; Shan, L.; Yang, H. Effects of In Situ TiB_2 on the Microstructural Evolution, Mechanical Properties, and Friction Behavior of the Al-Si-Cu Alloys Processed by Laser Powder-Bed Fusion. *Metals* **2024**, *14*, 1015. https://doi.org/10.3390/met14091015

Academic Editor: Pavel Krakhmalev

Received: 5 August 2024
Revised: 26 August 2024
Accepted: 28 August 2024
Published: 5 September 2024

1. Introduction

Additive manufacturing (AM) is a widely studied method that builds objects from the bottom up by adding materials in layers. Unlike traditional subtractive manufacturing, AM allows the direct creation of parts with intricate geometries, streamlining the production process, reducing cycle times, and cutting costs [1,2]. It also enables the production of light components without compromising strength. Laser powder-bed fusion (PBF-LB) is a key method in additive manufacturing that employs a high-energy laser beam to selectively melt metal powder layer-by-layer to create parts under a high cooling rate [3,4]. PBF-LB offers extensive design freedom and precise fabrication, making it pivotal in aerospace and

automobile manufacturing [5]. Currently, PBF-LB is predominantly utilized for shaping various metal materials, including high/medium-entropy alloys [6,7], stainless steel [8], etc. Aluminum (Al) alloys are preferred materials for PBF-LBed lightweight structures due to their excellent balance, low cost and density, excellent antioxidant properties, superior corrosion resistance, and effective thermal conductivity [9–11].

Cast Al-Si alloys exhibit excellent fluidity in a liquid state and demonstrate relatively small shrinkage during solidification, making them very suitable for PBF-LB manufacturing [12,13]. However, the moderate mechanical properties of Al-Si alloys limit the industrial applications in an extended range. Previous studies [14,15] have shown that the addition of Cu into Al alloys exerts a positive influence in strength enhancement. For example, the hardness of PBF-LBed AlSi10Mg with Cu addition reached a hardness level that the PBF-LBed Al7075 alloy obtained after T6 treatment. It has been suggested that the incorporation of 4 wt.% Cu in PBF-LBed AlSi10Mg alloy improves the nucleation rate of Al-Si eutectics and fosters the formation of the nano-Si phase during direct ageing, which achieves the ultrahigh yield strength of 522 MPa [15]. Apart from the increased solubility of Cu when induced by a high cooling rate at 10^3–10^6 °C/s, the non-equilibrium solidification process also promotes the formation of precipitation phases and builds the foundation of strengthening in Al-Si-Cu alloys with subsequent heat treatments [16,17].

Another approach to enhance the mechanical properties of PBF-LBed Al-Si-based alloys is to use composites by adding reinforcement particles. It has been found that Al-based composites can obtain excellent balance in good plasticity, good thermal conductivity, high stiffness, and excellent wear resistance [18,19]. The available and popular ceramic particles include Al_2O_3 [20], TiC [21], and TiB_2 [22]. Of these, TiB_2 offers extraordinary properties in combination, including (*i*) a high melting point that allows TiB_2 to remain stable in a melt pool [23], (*ii*) a high laser absorption rate and hardness that can enhance the formability and wear resistance of Al-based composites [24], and (*iii*) the coherent interface between α-Al matrix and TiB_2 particles that promotes grain refinement and improves mechanical properties [25]. It has been found that the optimal proportion of TiB_2 into an AlSi10Mg alloy can effectively inhibit crack propagation and acquire a superior combination of strength and ductility via eliminating the texture [26]. With diminishing metallurgical defects and improving the nucleation of α-Al grains, excellent mechanical properties (e.g., UTS of 390 ± 6.5 MPa and El of 14.8 ± 1.8%) could be obtained in the PBF-LBed TiB_2/Al-Cu-Mg-Ag composites [27]. Also, the hardness and wear resistance of a PBF-LBed Al7075 alloy are significantly increased when the content of TiB_2 particles increases continuously [28]. Also, the vertical section of a PBF-LBed TiB_2/Al-12Si composite consists of fine equiaxed grains [29]. TiB_2 particles can refine the coarse columnar grains and transform columnar grains into equiaxed grains in a PBF-LBed Al-12Si composite.

Previous work [30–32] has mainly concentrated on the effects of TiB_2 particles on Al-Cu and AlSi10Mg alloys. The studies include the role of TiB_2 particles in promoting the heterogeneous nucleation of α-Al grains and the impact of TiB_2 on the mechanical properties and strengthening effects of aluminum alloys processed by PBF-LB. However, the work on the influence of TiB_2 particles on the microstructure and mechanical properties of PBF-LBed Al-Si-Cu alloys is still limited even though Cu is critical in Al-Si alloys for improved mechanical properties. Therefore, the current research seeks to explore the effect of in situ TiB_2 particles on Al-Si-Cu alloys. The composite was made via the salt–metal reaction method. The microstructure and the mechanical and tribological properties of the PBF-LBed TiB_2/Al8SiCu alloy were thoroughly investigated. The discussion was concentrated on the strengthening mechanisms and wear mechanisms.

2. Materials and Experimental Procedures

2.1. Powder and Material Fabrication

The introduction of in situ TiB_2 nanometer-sized particles to Al-Si-Cu alloy was achieved using the mixed salt method with K_2TiF_6 and KBF_4 as reaction salts. The pre-alloyed ingots were supplied by industry. Gas atomization was utilized to fabricate Al8SiCu

and TiB_2/Al8SiCu pre-alloyed powders under argon protection. The elemental composition in Table 1 was determined using inductively coupled plasma atomic emission spectrometry (ICP-AES), revealing that the proportion of TiB_2 particles was 3.98 wt.%. The morphology and particle size distribution are depicted in Figure 1. The pre-alloyed powder showed high sphericity with minimal satellite attachments, and the TiB_2 particles were dispersed within the TiB_2/Al8SiCu composite powders. The size distribution of the Al8SiCu and TiB_2/Al8SiCu powders ranged from 11 to 62 µm with the average size of 30 µm. The TiB_2 particles were quite uniformly distributed throughout the matrix with minimal agglomeration (Figure 1(e_1–e_6)), and the distribution of the Ti element served as an indicator of the presence of TiB_2 within the powder composition. The powders were dried at 75 °C for 8 h in a vacuum oven and the substrate was preheated to 70 °C before processing by PBF-LB. The samples were fabricated at room temperature using the EP-M150 system equipped with an IPG Fiber Laser. The Al8SiCu and TiB_2/Al8SiCu alloys were processed using identical processing parameters: a laser power (P) of 230, 260, 290, and 320 W; a scanning speed (v) of 600, 800, 1000, 1200, and 1400 mm/s; a hatch spacing (h) of 0.1 mm; a layer thickness (t) of 0.03 mm; and a rotation angle of 67° between layers. The dimensions of the processed cube and rectangular samples were 10 mm × 10 mm × 10 mm and 84 mm × 12 mm × 10 mm, respectively.

Table 1. The chemical composition of the Al8SiCu powders and TiB_2/Al8SiCu composite powders.

Alloy (wt.%)	Si	Cu	Mn	Mg	Ti	B	Al
Al8SiCu	7.48 ± 0.03	1.42 ± 0.01	0.47 ± 0.01	0.40 ± 0.01	0.09 ± 0.02	/	Bal.
TiB_2/Al8SiCu	7.68 ± 0.03	1.40 ± 0.01	0.45 ± 0.01	0.39 ± 0.01	2.89 ± 0.02	1.24 ± 0.01	Bal.

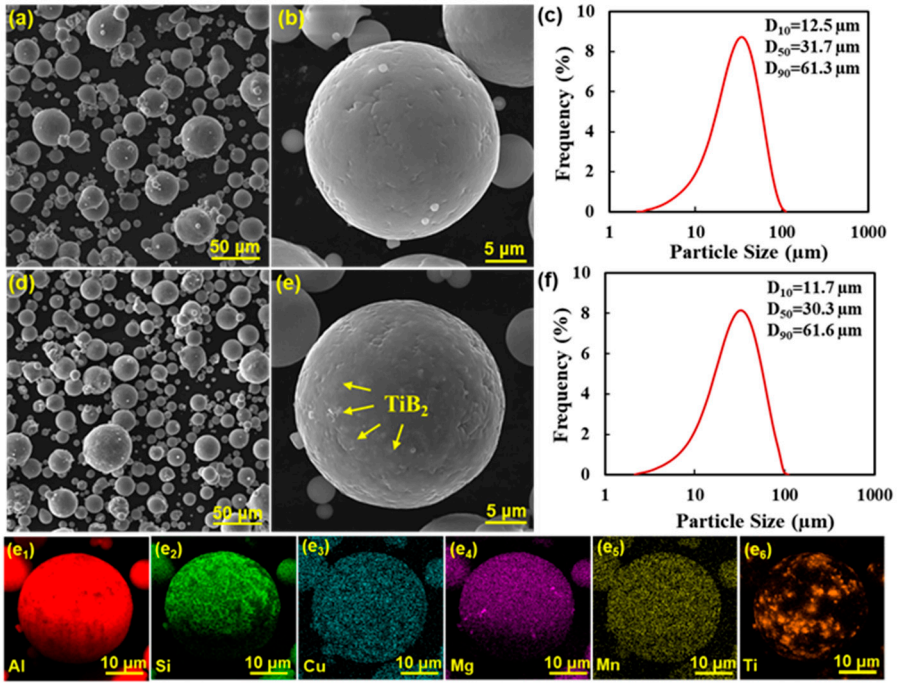

Figure 1. SEM images of the morphology (**a**,**b**) Al8SiCu powders, (**d**–**e**) TiB2/Al8SiCu composite powders (particle size distribution), (**c**) Al8SiCu powders, (**f**) TiB2/Al8SiCu composite powders, and (**e1**–**e6**) EDX maps of the images given in (**e**) showing the elemental maps for Al, Si, Cu, Mg, Mn, and Ti.

2.2. Microstructure Characterization

The phase composition of the PBF-LBed specimens was determined by X-ray diffraction technology (XRD) equipped with a Cu $K\alpha$ radiation setting in the 2θ range from 20° to

80°. The crystallographic database used in this work refers to the International Centre for Diffraction Data (ICDD) database. Meanwhile, the Rietveld analysis method was applied to calculate the quantities of each of the phases identified in the spectra. The drainage method was employed to assess the densification behavior. The surface defects were observed under an optical microscope (OM) after the samples were polished. The microstructure of the samples etched with Keller's reagent was observed with a scanning electron microscope (SEM) fitted with an energy-dispersive X-ray spectroscope (EDS) at an acceleration voltage of 20 kV. The grain size and orientation were investigated in terms of electron backscatter diffraction (EBSD) with a step size of 1.1 μm and an acceleration voltage of 20 kV, and the raw data were analyzed using TSL OIM 8.0 software. Disk-shaped samples prepared using the ion-thinning method were examined through transmission electron microscope (TEM) to further characterize and analyze the detailed microstructure. Additionally, the lattice strain (ε), dislocation density (δ), and lattice constant (D) of both the PBF-LBed Al8SiCu alloy and the PBF-LBed TiB_2/Al8SiCu composite listed in Table 2 were estimated based on XRD results. The calculation utilized the following formulas [33]:

$$D = K\lambda/(\beta \times \cos\theta) \quad (1)$$

$$\delta = 1/D^2, \quad (2)$$

$$\varepsilon = \beta/4 \times \tan\theta, \quad (3)$$

where K is a constant (0.9), β is the maximum value of the half-maximum width, λ is a constant related to the wavelength (0.15405 nm), D is the lattice constant, ε is the lattice strain, and θ is the diffraction angle.

Table 2. The lattice strain, dislocation density, and lattice parameter of the Al phase for the PBF-LBed Al8SiCu alloy and the TiB_2/Al8SiCu composite.

Sample	Lattice Strain	Dislocation Density	Lattice Parameter
Al8SiCu	2.87×10^{-3}	8.53×10^{14} m^{-2}	4.056 Å
TiB_2/Al8SiCu	3.01×10^{-3}	9.45×10^{14} m$_{-2}$	4.066 Å

2.3. Mechanical and Frictional Properties

The hardness was obtained by a micro-Vickers hardness tester with a 100 g load for 10 s. The average value was derived from the measurements taken at 8 separate points on each specimen. Dog-bone-shaped tensile samples fabricated through electric discharge wire-cutting technology were subjected to testing on a universal tensile testing machine with a strain rate of 1×10^{-3} s^{-1}. The tensile properties were determined by averaging the results from at least five specimens. Room temperature-reciprocating friction wear tests were conducted on the PBF-LBed samples using a ball-on-disk tribometer with GCr15 balls. The GCr15 ball applied a 7 N load to the specimens and performed reciprocating motion on its surface for 30 min. The motion speed and stroke length of the GCr15 ball were 40 mm/s and 12 mm, respectively.

3. Results

3.1. Densification Behavior

The relative density is a critical indicator for evaluating the densification effectiveness of PBF-LB. The volume energy density (*VED*) significantly determines the relative density of the samples manufactured by PBF-LB. The *VED* is usually described as in [34]: $VED = P/(vht)$. The relative densities of the PBF-LBed TiB_2/Al8SiCu composites and Al8SiCu alloys exhibited a similar trend of initial increase and then decrease when increasing the *VED*. The maximum relative densities of the Al8SiCu without and with TiB_2 addition were measured as 99.8% and 99.7%, respectively. The optimal *VED* range for achieving a relative density above 99.5% was found between 56.2 J/mm^3 and 91.6 J/mm^3 for the TiB_2/Al8SiCu

composite and 68.7 J/mm^3 and 94.8 J/mm^3 for the Al8SiCu alloy. Clearly, the addition of in situ TiB_2 not only lowered the optimal *VEDs* for high-density Al8SiCu alloys, but it also expanded the range of the process parameters for PBF-LB process. Meanwhile, the OM results in Figure 2b indicate that low *VEDs* resulted in incomplete powder melting and poor density (Figure 2(b1,b4)). The powders were fully melted and exhibited good wettability as the *VED* increased, and only small pores were observed in the good samples (Figure 2(b2,b5)). However, further elevations of *VED* triggered intensive convection within the melt pool and caused element evaporation, leading to the formation of more holes. Also, the presence of TiB_2 enhanced the laser absorption rate of the pre-alloyed powders and made the melt pool more unstable at high *VEDs*, resulting in more pinholes in the TiB_2/Al8SiCu composite (Figure 2(b3,b6)).

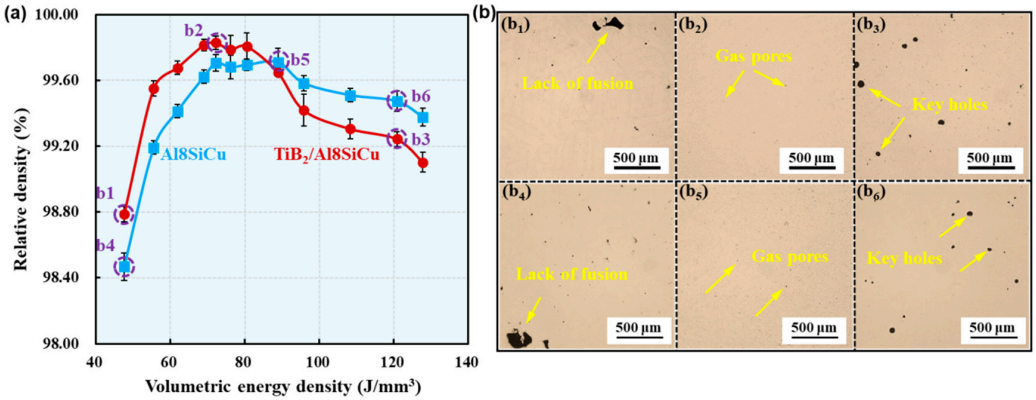

Figure 2. (**a**) The effect of the volumetric energy density on the relative density, (**b**) optical micrographs showing the defects in the horizontal direction at different volume energy densities in (**b$_1$**–**b$_3$**) the PBF-LBed TiB_2/Al8SiCu composite, and (**b$_4$**–**b$_6$**) the PBF-LBed Al8SiCu alloy.

3.2. Phase Analysis

The XRD spectra for the phase analysis in the PBF-LBed TiB_2/Al8SiCu composite and Al8SiCu alloy are shown in Figure 3. The α-Al phase and Si phase were detected in both samples, and the TiB_2 peak was only detected in the TiB_2/Al8SiCu composites. The quantities of the α-Al phase and Si phase in Al8SiCu were 92.5 wt.% and 7.5 wt.%, respectively. In TiB_2/Al8SiCu, the quantities of the α-Al phase, Si phase, and TiB_2 were 88.9 wt.%, 6.8 wt.%, and 4.3 wt.%, respectively. Also, Al_3Ti and Al_2B phases were not found in the composites, indicating that the TiB_2 was stable in the composite and that were was no decomposition or the formation of metastable phases. Also, no Mg- and/or Cu-enriched phases were observed in the XRD spectra, indicating the complete dissolution of these solute elements into the matrix (Figure 3a). Meanwhile, the introduction of TiB_2 induced a shift of the Al peaks toward lower diffraction angles, suggesting an expansion in the lattice constant of Al in accordance with Bragg's law (Figure 3b). It was anticipated that the enlargement of the lattice constant was associated with the increased dissolution of Mg and Cu elements under a high cooling rate in PBF-LB [35]. Additionally, the strongest $(200)_{\alpha\text{-Al}}$ peak in the PBF-LBed Al8SiCu alloy implied the preferred crystallographic orientation during the PBF-LB process. But the intensity of $(200)_{\alpha\text{-Al}}$ peak was weakened in the TiB_2/Al8SiCu composite, suggesting that TiB_2 might inhibit the growth of Al grains in a preferred direction (Figure 3b).

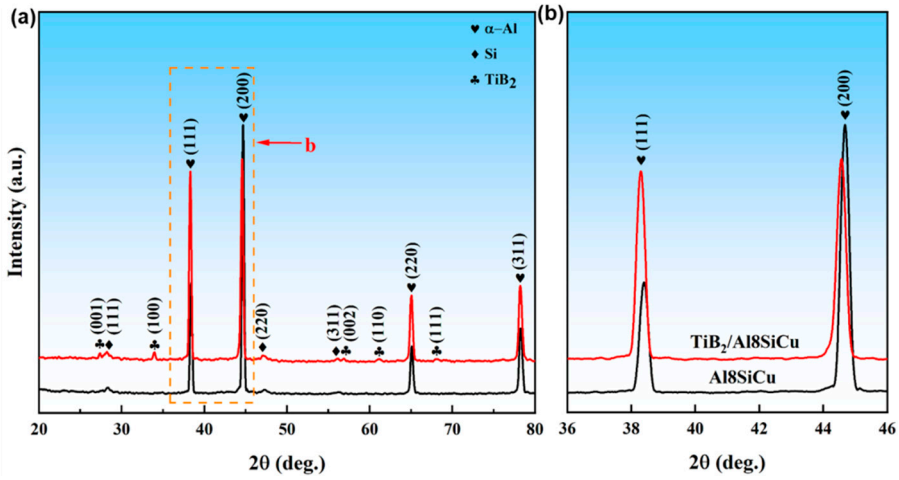

Figure 3. (**a**) The XRD spectra for the phase analysis in the PBF-LBed TiB2/Al8SiCu composite and Al8SiCu alloy samples (**b**) the enlargement of Al peak from 36° to 46°.

According to the XRD data and Formulas (1)–(3), it was also observed that the lattice parameter, dislocation density, and lattice strain of the PBF-LBed TiB_2/Al8SiCu composites were all higher than those of the PBF-LBed Al8SiCu alloy (Table 2). The incorporation of TiB_2 led to the enlargement of the α-Al lattice parameter while also inducing an increase in the dislocation density. The increase in dislocation density enhanced the mechanical properties of the TiB_2/Al8SiCu composite.

3.3. Microstructural Characterization

Non-equilibrium solidification is the key feature in the PBF-LB process, resulting in an increase in the solubility of the solute elements and the formation of melting pools containing a cellular structure in the two experimental materials (Figure 4). Similar to the observations of the cellular structures for other alloys [36], the melt pool was composed of a fine zone (FZ), heat-affected zone (HAZ), and coarse zone (CZ) in the TiB_2/Al8SiCu composite and the Al8SiCu alloy. Also, TiB_2 particles were observed within the α-Al cells and at the cell boundaries, with sizes ranging from 100 nm to 3 μm in the TiB_2/Al8SiCu composite. During solidification under a high cooling rate, the α-Al phase was precipitated first, and then the Si and other solutes accumulated in front of the solid/liquid interface and segregated along the cell boundaries [37], as shown in Figure 4b,d. The fine precipitates were observed within the supersaturated α-Al cells. As can be seen in Figure 4, the addition of TiB_2 particles had little effect on the α-Al cellular structure but significantly refined the grains. The changes in the grain and detailed microstructural characteristics will be investigated in the following sections.

Figure 5 shows that EBSD results of the PBF-LBed Al8SiCu alloy and TiB_2/Al8SiCu composite in a building direction. It was observed that the TiB_2 promoted a columnar to equiaxed transition (CET) of the α-Al grains in the PBF-LBed Al8SiCu alloy. The texture was 2.081 in the microstructure of the Al8SiCu alloy with the feature of columnar crystals and fine equiaxed crystals distributed at the melt pool boundaries. During the PBF-LB process, the temperature gradient (G) and the solidification rate (R) affected the grain morphology and grain size. The ratio G/R was confirmed to control the grain morphology of the microstructure, and the $G \times R$ determined the grain size. At the bottom of the melt pools, a lower G/R ratio resulted in the formation of fine equiaxed crystals at the boundaries of the pool [38]. The steep thermal gradient within the melt pools led to the growth direction of the columnar crystals being the almost aligned with the vertical direction, and most of these were along the <001> direction, which was consistent with the XRD results (Figure 3a). Due to the layer-by-layer accumulation and melting, some of the coarse columnar crystals would penetrate into another melting pool. Clearly, no coarse columnar crystals were detected in the PBF-LBed TiB_2/Al8SiCu composite. The size of the columnar crystals was

significantly decreased with a weak average texture intensity (1.76), suggesting the random grain orientation was strengthened. The obvious CET induced via TiB_2 addition promoted the grain refinement in the Al8SiCu alloy, of which the average grain size decreased from 15.31 μm to 7.34 μm (Figure 5c,d). Moreover, the addition of TiB_2 generated a high fraction of high-angle grain boundaries (HAGBs > 15°, Figure 5e,f). The HAGBS were known as the barriers to dislocation motion and thus could enhance the mechanical properties [39]. Further analysis of the grain aspect ratio is presented in Figure 5g,h. The ratio of length to width was used to define the aspect ratio. For clarity, grains with aspect ratios below 2 were classified as equiaxed grains, those between 2~4 as columnar grains, and those above 4 as coarse columnar grains. Clearly, the existence of TiB_2 elevated the proportion of the equiaxed crystals from 36.3% to 49.9% and decreased the fraction of the coarse columnar crystals from 21.2% to 11.6%.

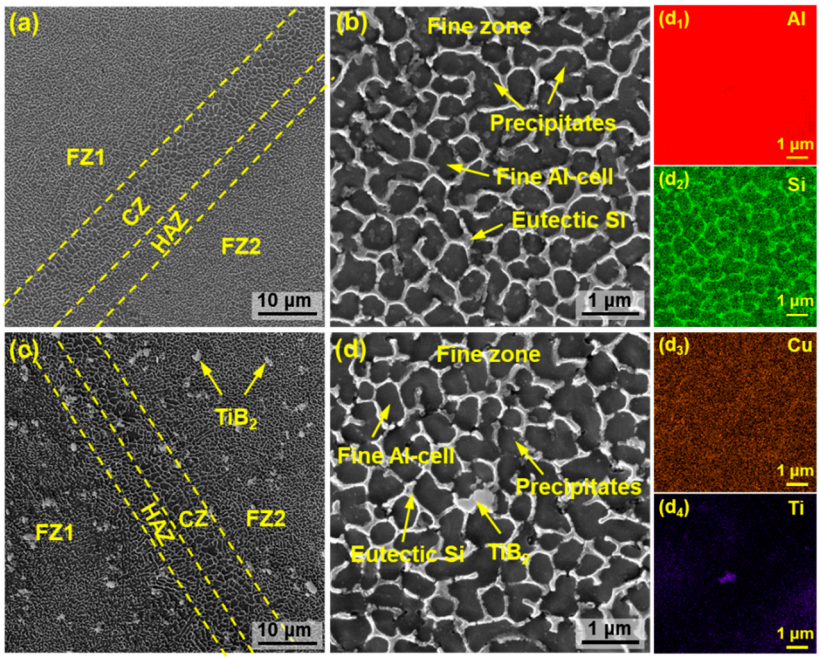

Figure 4. SEM images showing the microstructure of (**a**,**b**) the PBF-LBed Al8SiCu alloy, (**c**,**d**) the PBF-LBed TiB_2/Al8SiCu composite, (**d_1**–**d_4**) and EDX maps of the images in (**d**) showing the elemental maps for Al, Si, Cu, and Ti.

Detailed microstructural characteristics of the PBF-LBed Al8SiCu alloy without and with TiB_2 addition are shown in Figures 6 and 7. Bright field TEM (BF-TEM) images showed that the microstructure of the PBF-LBed Al8SiCu alloy featured cellular structures (Figure 6a), similar to the observations in Figure 4. The interaction between a high number density of precipitates and dislocations was also observed within the cellular structures (Figure 6b,c). Elemental results calibrated in Figure 6c demonstrated that the Si phases were the main precipitates, as verified by the Si segregation along the cellular structure boundaries. The β-Mg_2Si phase and the θ-Al_2Cu phase were identified by the enrichment of Mg, Si, and Cu in Figure 6 (c_2–c_4). The orientation relationships between the α-Al matrix and β-Mg_2Si phase/β″ phase was determined via high-resolution TEM (HR-TEM) and fast Fourier transform (FFT) images, as shown in Figure 6d–f. The orientation relationship between the Si phase and α-Al could be expressed as follows: $(200)_{\alpha\text{-Al}}//(\bar{1}11)_{Si}$, $(220)_{\alpha\text{-Al}}//(311)_{Si}$, and $[001]_{\alpha\text{-Al}}//[\bar{1}12]_{Si}$. The $(00\bar{1})$ plane of the β″ phase was found parallel to the (020) plane of α-Al, forming a semi-coherent interface. Also, the HR-TEM micrographs and corresponding FFT images shown in Figure 6f further confirmed the presence of the β-Mg_2Si phase at the cellular structures, of which the β phase possessed a coherent orientation with the α-Al matrix. The $[\bar{1}12]$ axis of the β-Mg_2Si phase was parallel

to the [001] axis of α-Al, and the summarized orientation relationships are shown below ($(\bar{1}11)_{\beta}//(020)_{\alpha-Al}$, $(220)_{\beta}//(200)_{\alpha-Al}$).

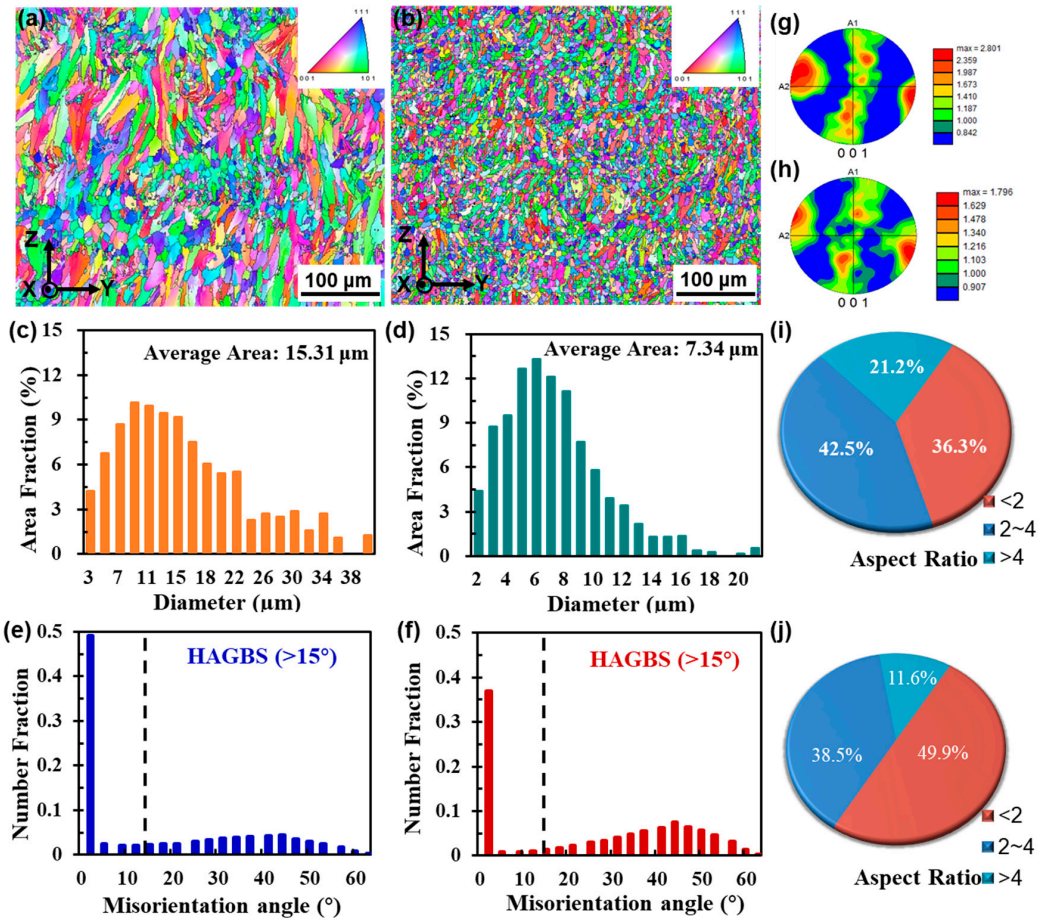

Figure 5. EBSD map results of the as-PBF-LBed (**a**,**c**,**e**,**g**,**i**) Al8SiCu and (**b**,**d**,**f**,**h**,**j**) as-PBF-LBed TiB_2/Al8SiCu samples in a building direction. (**a**,**b**) Inversed pole figures, (**c**,**d**) grain-size distribution, (**e**,**f**) misorientation angle distribution, (**g**,**h**) pole figures, and (**i**,**j**) aspect ratio.

Similar to the Al8SiCu alloy, the interaction between precipitates and dislocation was detected within the Si eutectics in the PBF-LBed TiB_2/Al8SiCu composite (Figure 7a–c). The EDS results shown in Figure 7(c_1–c_6) confirmed that the nanoscale precipitates were Si phases. The interaction between the tangled dislocations and β-Mg_2Si phase/θ-Al_2Cu phase was also detected at the vicinity of TiB_2 particles. The precipitates and dislocations interacted with each other, generating elastic stress fields that hindered the migration of dislocations and increased the strength of the composite. BF-TEM images of prismatic TiB_2 with a size of 100 nm and inserted SAED patterns are displayed in Figure 7d. The HAADF-STEM image in Figure 7e,f shows in situ particles within the cellular structure. The corresponding elemental distribution confirmed that the precipitates were in a Si phase and Al_2Cu phase. Also, the selected area electron diffraction (SAED) indicated that the orientation relationship between the Al and θ- Al_2Cu phases was identified as follows: $[0\bar{1}1]_{\alpha\text{-}Al}//[101]_{\theta}$ and $(\bar{1}\bar{1}1)_{\alpha\text{-}Al}//(020)_{\theta}$ (Figure 7f).

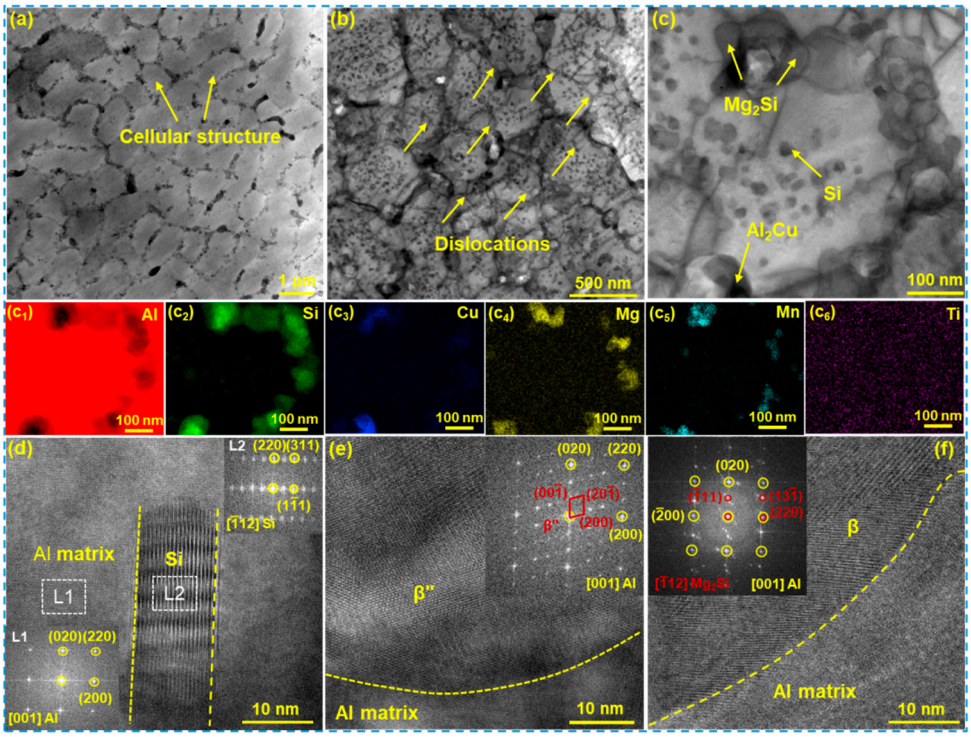

Figure 6. TEM images of the PBF-LBed Al8SiCu alloy: (**a**) BF-TEM image of the cellular structure; (**b**) high-density dislocation with the cellular structure; (**c**) an overview of the precipitate distribution in the cellular structure and corresponding mapping of the main elements of Al, Si, Cu, Mg, Mn, and Ti (**c_1**–**c_6**); (**d**) HRTEM micrograph and corresponding SAED patterns showing the Si phase; (**e**) HRTEM micrograph and corresponding SAED patterns showing the β″ phase; and (**f**) HRTEM micrograph and corresponding SAED patterns showing the β-Mg_2Si phase.

The detailed characteristics of interface between the submicron TiB_2 particles and the Al matrix are displayed in Figure 8. The TiB_2 particle showed a good relationship with the Al matrix, with the enrichment of Al, Ti, and Si segregated at the transition layer (Figure 8b). The EDX line profiles in Figure 8c further confirmed the presence of the Al-Ti layer at the TiB_2/α-Al interface, which is consistent with previous research conclusions [40]. The presence of the Al-Ti layer has been confirmed to be able to promote the heterogeneous nucleation of TiB_2 particles [41]. However, the presence of Si at the interface causes the Al-Ti layer to lose its ability to promote the nucleation of TiB_2 particles. Although the poisoning effect of Si inhibits the nucleation of TiB_2 particles, most of the TiB_2 particles can still play a role during the heterogeneous nucleation of α-Al due to their high content and predominantly nanoscale size.

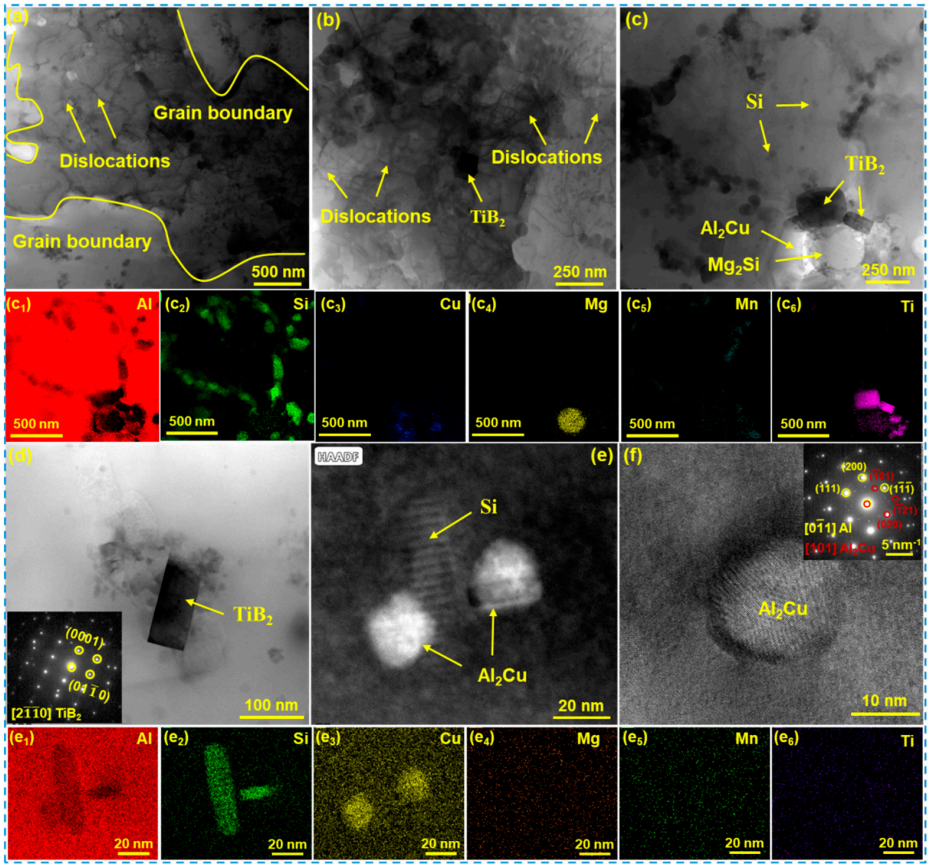

Figure 7. TEM images of the PBF-LBed TiB_2/Al8SiCu composite: (**a**) BF-TEM image showing the cellular structure and grain boundary, (**b**) the interaction between dislocations and particles, (**c**) an overview of the precipitate distribution in the cellular structure and the elemental mapping of Al, Si, Cu, Mg, Mn and Ti (**c$_1$**–**c$_6$**), (**d**) BF-TEM image showing the morphology of TiB_2 and the SAED patterns of TiB_2, (**e**) HAADF-STEM image showing the Si phase and Al_2Cu phase, as well as corresponding mappings of the main elements of Al, Si, Cu, Mg, Mn, and Ti (**e$_1$**–**e$_6$**), and (**f**) HRTEM micrograph showing the Al_2Cu phase (the inset is the corresponding SAED patterns).

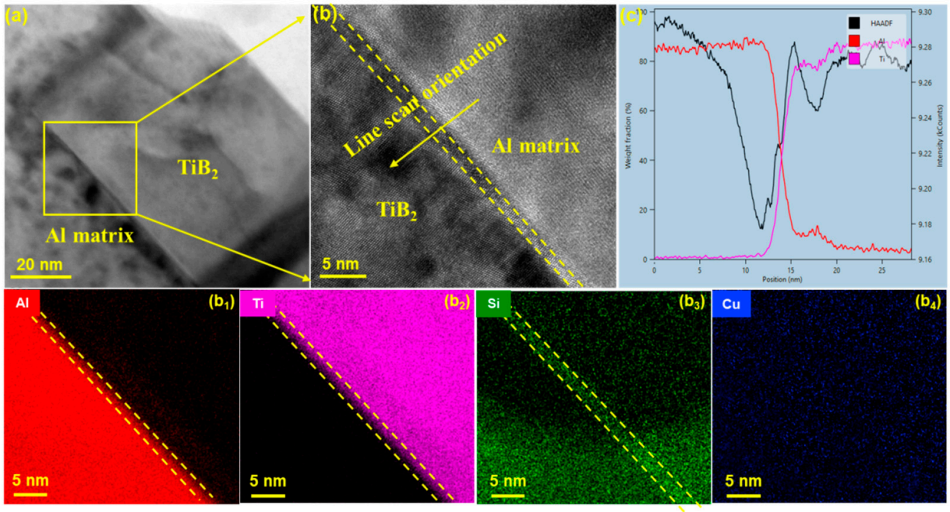

Figure 8. (**a**) BF-TEM image showing the submicrometric-sized TiB2 particles, (**b**) HRTEM image showing the interface of Al/TiB2 and the corresponding STEM EDX mapping of Al, Ti, Si and Cu (**b$_1$**–**b$_4$**), and (**c**) EDX line profiles across the interface showing an interphase rich in Al and Ti elements.

3.4. Mechanical Properties

Figure 9a illustrates the engineering stress–strain curves of the PBF-LBed Al8SiCu alloy without and with TiB_2 addition, and the corresponding tensile properties are illustrated in Figure 9b. The Al8SiCu alloy and the TiB_2/Al8SiCu composite initially underwent elastic deformation followed by yielding and strain hardening before fracturing. The enhanced strain hardening capability was observed in the TiB_2/Al8SiCu composite, which was primarily ascribed to the abundant dislocation loops distributed within cellular structures [42]. The yield strength (YS), ultimate tensile strength (UTS), and elongation (El) of the PBF-LBed Al8SiCu alloy were 296 ± 6 MPa, 517 ± 6 MPa, and 11.7 ± 1.0%, respectively. The addition of TiB_2 particles enhanced the strength with a slight reduction in elongation, of which the UTS, YS, and El were 328 ± 8 MPa, 541 ± 3 MPa, and 9.1 ± 0.7%, respectively.

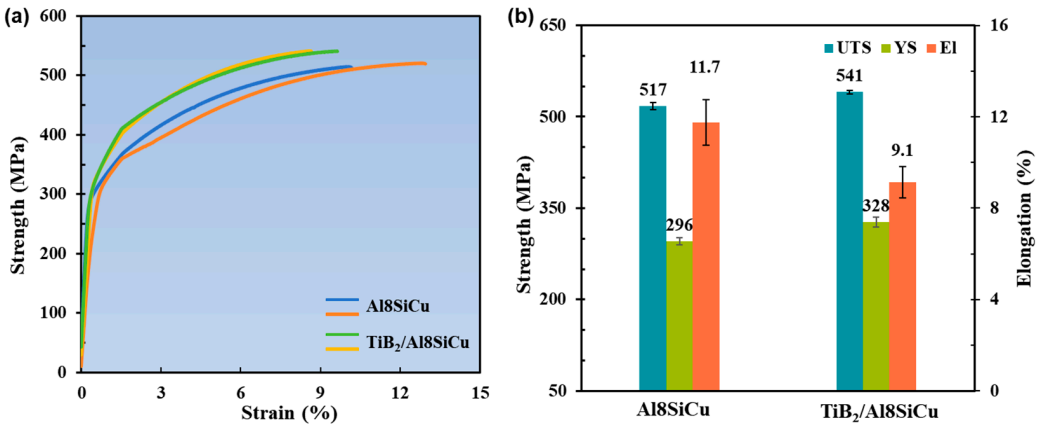

Figure 9. (**a**) Stress–strain curves and (**b**) the tensile of the PBF-LBed Al8SiCu alloy and the PBF-LBed TiB_2/Al8SiCu composite.

The fractured morphology shown in Figure 10 indicated that a large number of dimple structures and a few cleavage steps were observed on the fractured surfaces of both the Al8SiCu alloy and the TiB_2/Al8SiCu composite, suggesting a mixed mode of ductile and brittle fracture patterns. Meanwhile, a large number of pores ranging from 5–15 μm were detected on the fractured surface of the TiB_2/Al8SiCu composite because of the interfacial debonding between the TiB_2 particles and the α-Al matrix during tensile process [43], while the micrometer-scale small pores at the fractured surface of the Al8SiCu alloy were highly associated with the non-escaping gas in time during the PBF-LB solidification process [44]. Clearly, a high number density of pores and partially agglomerated TiB_2 particles resulted in a low poor elongation for the TiB_2/Al8SiCu composite as a counterpart with the Al8SiCu alloy.

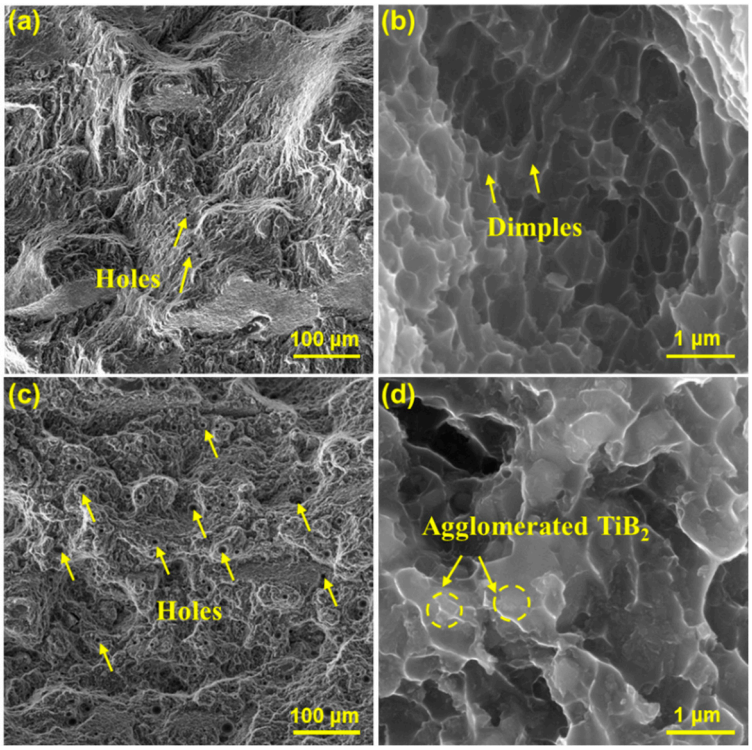

Figure 10. Fracture morphology of (**a**,**b**) the Al8SiCu alloy and (**c**,**d**) the TiB_2/Al8SiCu composite.

3.5. Tribological Behavior

The addition of ceramic particles with high hardness normally improves the wear resistance of metallic materials [45,46]. Figure 11 shows the friction coefficient, the wear-off rate, and the hardness of the PBF-LBed Al8SiCu alloy and the PBF-LBed TiB_2/Al8SiCu composite. Initially, the friction coefficient experienced notable fluctuations due to the insufficient contact between the milling ball and the samples. With the increase in friction time, the friction coefficient gradually stabilized and maintained no change for the experimental time. The calculated data revealed that the Al8SiCu alloy had an average friction coefficient of 0.655 and a wear rate of 1.76×10^{-3} mm^3/Nm, while the TiB_2/Al8SiCu composite had a lower average friction coefficient of 0.580 and a reduced wear rate of 1.38×10^{-3} mm^3/Nm. The TiB_2 addition reduced the average friction coefficient by 11.4% and the wear rate by 21.5%.

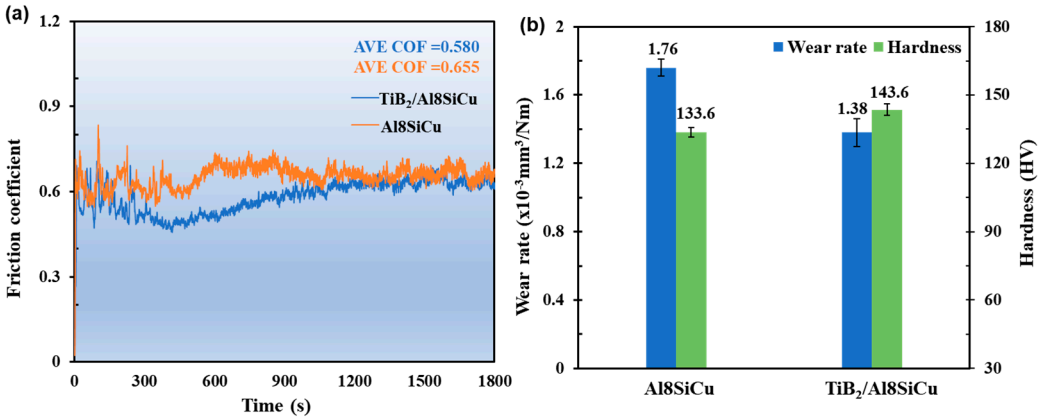

Figure 11. (**a**) Friction coefficient vs. time, and the (**b**) wear-off rate and hardness of the PBF-LBed Al8SiCu alloy and the PBF-LBed TiB_2/Al8SiCu composite.

Figure 12 shows the morphology of the worn surfaces of the PBF-LBed Al8SiCu alloy and TiB_2/Al8SiCu composite. It was observed that the rough worn surface was featured by deep ploughing grooves in the PBF-LBed Al8SiCu alloy (Figure 12a). Some severe worn areas also showed fragmentation and peeling and the existence of grooves and pits (Figure 12b), indicating the poor wear resistance and adhesive wear mechanism of the PBF-LBed Al8SiCu alloy. In the counterpart of the TiB_2/Al8SiCu composite, only a low density of the thinner/shallower grooves and a high density of wear debris were detected at the worn surface. During the friction test, the hard TiB_2 particles that possessed a good interfacial relationship with the α-Al matrix did not easily fall off during the testing. Therefore, the frictional force and the wear rate were correspondingly reduced in the TiB_2/Al8SiCu composite. Meanwhile, TiB_2 particles were disengaged from the matrix and generated wear debris on the wear track surface as the friction time was prolonged, prompting a shift to a combined wear mechanism of abrasive and adhesive wear (Figure 12d). Moreover, the incorporation of TiB_2 particles resulted in an evident grain refinement that enhanced the load-bearing capacity of the TiB_2/Al8SiCu composite, which effectively inhibited the initiation of cracks during friction.

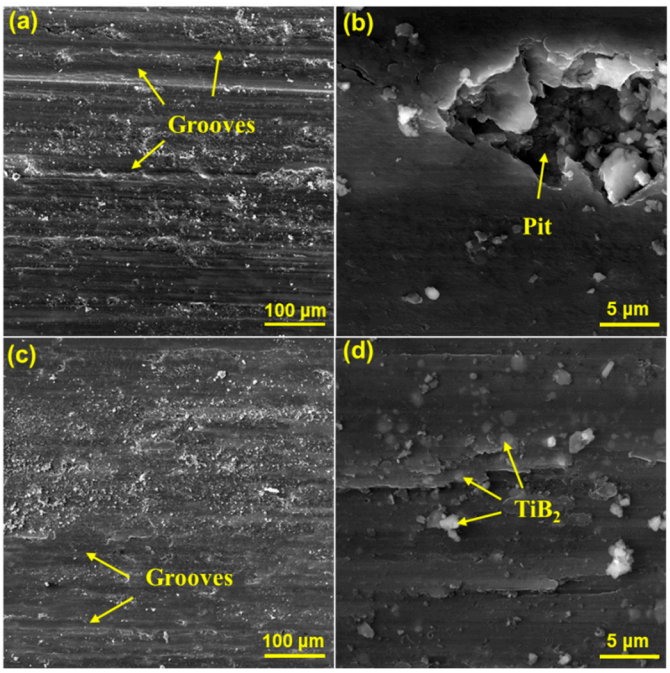

Figure 12. SEM images showing the morphology of the worn surfaces of (**a**,**b**) the PBF-LBed Al8SiCu alloy and (**c**,**d**) the PBF-LBed TiB_2/Al8SiCu composite.

4. Discussion

4.1. Effect of In-Situ TiB_2 Particles on Microstructural Evolution

Referring to the results mentioned above, the introduction of an addition of in situ TiB_2 offered the following positive influence: (1) The addition of TiB_2 increased the laser absorption rate of the powder and achieved a high relative density under lower *VED* conditions. (2) The refinement of the composite microstructure and the well-fitted interface between the TiB_2 particles and the Al matrix resulted in significant improvements in the mechanical and friction properties. (3) The TiB_2 particles provided effective nucleation sites for α-Al grains and promoted the CET. Consequently, the microstructure was refined in the PBF-LBed composite. Schematic diagrams of the microstructural characteristics of the PBF-LBed Al8SiCu alloy and TiB_2/Al8SiCu composite are shown in Figure 13. It was observed that the preliminary solidified areas underwent partial remelting during PBF-LB, which led to epitaxial grain growth in the Al8SiCu alloy, which formed columnar crystals (Figures 5a and 13a). However, an obvious CET effect can be achieved after the

precipitation of TiB_2, of which the TiB_2/Al8SiCu composite was characterized by equiaxed grains (Figures 5b and 13b).

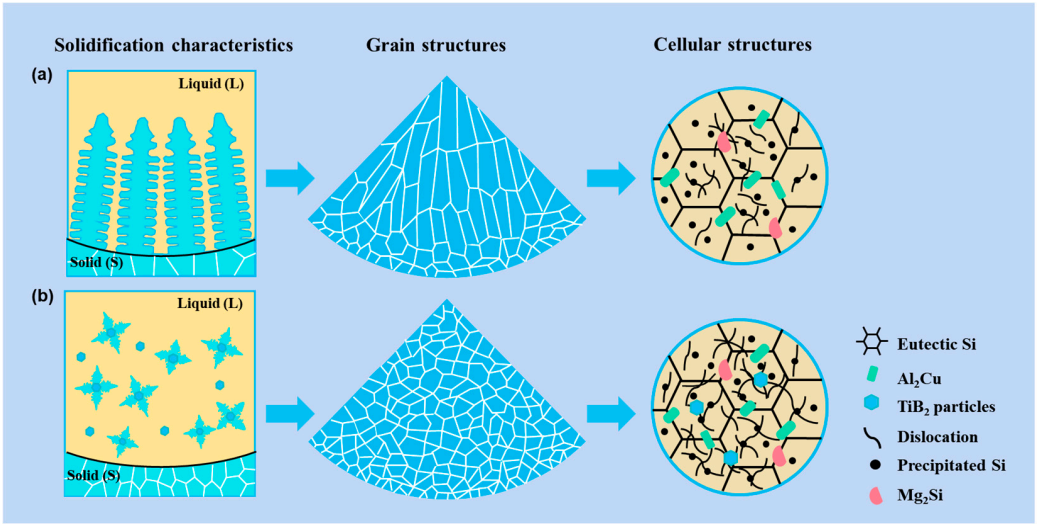

Figure 13. Schematic diagram showing the development in the microstructure of (**a**) the PBF-LBed Al8SiCu alloy and (**b**) the PBF-LBed TiB_2/Al8SiCu composite.

To achieve effective grain refinement, the ceramic particles must not only maintain a favorable interface with α-Al, but also uniformly distribute in the entire melted pools. The TiB_2 particles showed a good orientation relationship with the Al matrix (Figure 8b), and this also increased the laser absorption in improving the energy in the melt pool, which causes intensive Marangoni convection, which improves the distribution of TiB_2 particles in the melted pools [47]. It was also noted that the Ti atoms were initially adsorbed on the {0001} plane of TiB_2 during solidification, which led to the formation of the typical Al-Ti layer, as well as reductions in the lattice mismatch between the TiB_2 and the α-Al matrix (from 4.22% to 0.09%) [48,49]. Correspondingly, the uniformly distributed TiB_2 particles that possessed a low lattice mismatch with the α-Al matrix were able to exert a positive influence in increasing the heterogeneous nucleation rate and promoting grain refinement [50]. Although previous studies [51] have indicated that a small fraction of TiB_2 particles are effective in heterogeneous nucleation, the majority of the TiB_2 particles effectively limited the epitaxial growth of grains, further leading to grain refinement and the formation of equiaxed crystals [52]. Last but not least, the in situ TiB_2 particles that possessed a large difference in thermal expansion coefficient with α-Al matrix promoted an increase in dislocation density within the cellular structure, which builds a solid foundation for strength enhancement (Figure 9).

4.2. Effect of In-Situ TiB_2 Particles on Strengthening Mechanisms

As shown in Figure 9, the incorporation of TiB_2 into the Al8SiCu alloy enhanced the yield strength at a level of 328 MPa. The yield strength of the TiB_2/Al8SiCu composite mainly originates from the following strengthening mechanisms: grain boundary strengthening (σ_g), dislocation strengthening (σ_{dis}), load-bearing strengthening (σ_{load}), Orowan strengthening (σ_{Orowan}), and solid solution strengthening (σ_{ss}). The formula for estimating the yield strength is as follows:

$$\sigma = \sigma_g + \sigma_{dis} + \sigma_{load} + \sigma_{Orowan} + \sigma_{ss}. \quad (4)$$

Compared to the average grain size of the Al8SiCu alloy (15.31 μm), the average grain size of the TiB_2/Al8SiCu composite was significantly reduced (7.34 μm), increasing the abil-

ity to hinder the dislocation movement. The contribution of grain boundary strengthening to the strength of the TiB_2/Al8SiCu composite can be calculated as follows:

$$\sigma_g = \sigma_0 + K \times {d_c}^{-1/2}, \tag{5}$$

where σ_0 is the lattice friction strength (20 MPa), K is the Hall–Petch coefficient (0.14 MPa $m^{1/2}$) [16], and d_c is the average grain size of the TiB_2/Al8SiCu composite (7.34 μm). Therefore, the contribution of the grain boundary strengthening to strength was approximately 71.7 MPa.

The data in Table 2 were obtained through a calculation of the XRD test results. The dislocation density of the Al8SiCu alloy was 8.53×10^{14} m^{-2}, while the dislocation density (ρ_c) of the TiB_2/Al8SiCu composite was 9.45×10^{14} m^{-2}. Due to the difference in the coefficients of thermal expansion between Al (23.5×10^{-6} K^{-1}) and TiB_2 (7×10^{-6} K^{-1}), the dislocation density at the TiB_2/Al interface increased. The contribution of the dislocation strengthening to the strength of the TiB_2/Al8SiCu composite can be calculated as follows:

$$\sigma_{dis} = M\beta G_m b {\rho_c}^{\frac{1}{2}}, \tag{6}$$

where M is the Taylor factor (3.06 for the FCC crystal structure of Al), β is the dislocation strengthening coefficient (0.16), G_m is the shear modulus (26.5 GPa), and b is the Burgers vector (0.286 nm) [11]. Consequently, the strength attributed to dislocation strengthening was about 114.1 MPa.

The TiB_2 particles had a good interface relationship with the aluminum matrix, allowing the load to be transferred from the aluminum matrix to the TiB_2, which led to an increase in yield strength. The contribution of the load-bearing strengthening can be expressed as follows [29]:

$$\sigma_{load} = 1.5 V_p \sigma_m, \tag{7}$$

where V_p is the volume fraction of TiB_2 particles (2.3 vol%) and σ_m is the bonding strength between the TiB_2 particles and the Al-Si matrix (~676 MPa [17]); thus, the contribution of the load-bearing strengthening mechanism to the strength was 23.3 MPa.

In the TiB_2/Al8SiCu composite, the reciprocal scanning of the laser during the PBF-LB process resulted in a significant precipitation of the nano-Si phases within the cellular structure. The nano-Si phases within the cells contributed to Orowan strengthening. Since most of the TiB_2 was mainly distributed at the grain boundaries or cell boundaries, the contribution of the TiB_2 particles to Orowan strengthening was minimal and can be neglected. The strength contribution from the Orowan strengthening mechanism can be calculated as follows [14]:

$$\sigma_{Orowan} = \frac{\varphi G_m b}{d_p} \left(\frac{6V_p}{\pi} \right)^{1/3}, \tag{8}$$

where φ is a constant 2, G_m is the shear modulus (26.5 GPa), b is the Burgers vector (0.286 nm), V_p is the volume fraction of the Si particles within the coarse Si eutectic networks (3.2 vol%), and d_p is the average size of the Si particles (80 nm). The values of V_p and d_p were obtained through the analysis of TEM images using ImageJ 1.53 software. The contribution of the Orowan strengthening to the strength was approximately 74.6 MPa.

During the PBF-LB process, the high cooling rate caused the solubility of the Si, Cu, Mg elements in the Al matrix to far exceed their equilibrium solubility limits, resulting in excellent solid solution strengthening. The contribution of the solid solution strengthening can be calculated using the following formula:

$$\sigma_{ss} = k_{Cu} C_{Cu}^m + k_{Si} C_{Si}^m + k_{Mg} C_{Mg}^m, \tag{9}$$

where k_{Cu}, k_{Si}, k_{Mg}, and m are 13.8 MPa/wt.%, 11 MPa/wt.%, 18.6 MPa/wt.%, and 1, respectively [53]; and C_{Cu}, C_{Mg}, and C_{Si} are the concentration of Cu, Mg, and Si in the solution, respectively. According to the results of the EDS measurement, the values of C_{Cu},

C_{Mg}, and C_{Si} were 3.57 wt%, 1.23 wt%, and 0.26 wt%, respectively. The contribution of the solid solution strengthening to the strength was approximately 61.1 MPa.

$$\sigma = \sigma_g(71.7) + \sigma_{dis}(114.1) + \sigma_{load}(23.3) + \sigma_{Orowan}(74.6) + \sigma_{ss}(61.1).$$

The value of σ (344.8 MPa) calculated from the formula was slightly greater than the result measured by mechanical performance tests (328 MPa). The excessive increment may have resulted from the volume fraction of the nano-Si phase used in Formula (8) exceeding the actual volume fraction of the precipitated Si phase in the TiB_2/Al8SiCu composite, leading to an overestimation of the Orowan strengthening.

5. Conclusions

In this study, a systematic study was conducted on the parameter optimalization, microstructural evolution, mechanical properties, and friction characteristics of the Al8SiCu alloy without and with in situ TiB_2 particles. The main conclusions can be drawn as follows:

(1) The addition of in situ TiB_2 particles into Al8SiCu alloys reduces the volumetric energy density required for the high-density TiB_2/Al8SiCu composite. Meanwhile, TiB_2 particles promote the transformation from columnar to equiaxed crystals and the formation of high-angle grain boundaries. The grains on the vertical direction of the PBF-LBed TiB2/Al8SiCu composite are much smaller than those of the PBF-LBed Al8SiCu alloy.

(2) The yield strength (YS), ultimate tensile strength (UTS), and elongation (El) of the PBF-LBed Al8SiCu alloy were 296 $\pm$ 6 MPa, 517 $\pm$ 6 MPa, and 11.7 $\pm$ 1.0%, respectively. The PBF-LBed TiB_2/Al8SiCu composite achieved a balance between the strength and the ductility, with the yield strength of 328 $\pm$ 8 MPa, an ultimate tensile strength of 541 $\pm$ 3 MPa, and an elongation of 9.1 $\pm$ 0.7%. The increase in strength primarily resulted from grain boundary strengthening, dislocation strengthening, load-bearing strengthening, solid solution strengthening, and Orowan strengthening, of which the dislocation strengthening and Orowan strengthening were critical in the strengthening.

(3) The enhanced hardness resulting from the refinement of grains and the presence of in situ TiB_2 particles also led to lower friction coefficients and wear off rates, which, in turn, enhanced the wear resistance behavior.

Author Contributions: Conceptualization: J.Z., L.S., S.J., M.Z., F.Y., T.W. Methodology: J.W., M.Z., F.Y., T.W. Software: M.Z., T.W. Validation: Z.H., F.Y. formal analysis: Z.H., M.Z. Investigation: Z.H., M.Z., F.Y. Resources: H.Y., S.J. data curation: Z.H., F.Y. writing—original draft preparation: Z.H. writing—review and editing: S.J., H.Y., J.W. Visualization: Z.H., S.J. supervision: H.Y., S.J. project administration: H.Y., S.J. Funding acquisition: J.Z., L.S. All authors have read and agreed to the published version of the manuscript.

Funding: This work was financially supported by the National Natural Science Foundation of China (Grant No. 52071343) and the Leading Innovation and Entrepreneurship Team of the Zhejiang Province-Automotive Light Alloy Innovation Team (No. 2022R01018).

Data Availability Statement: Data is contained within the article.

Conflicts of Interest: Author Jianming Zheng and Ling Shan was employed by the company Zhejiang Wanfeng Precision Casting Co., Ltd. The remaining authors declare that the research was conducted in the absence of any commercial or financial relationships that could be construed as a potential conflict of interest.

References

1. DeRroy, T.; Mukherjee, T.; Milewski, J.O.; Elmer, J.W.; Ribic, B.; Blecher, J.J.; Zhang, W. Scientific, technological and economic issues in metal printing and their solutions. *Nat. Mater.* **2019**, *18*, 1026–1032.
2. Ahmed, N. Direct metal fabrication in rapid prototyping: A review. *J. Manuf. Process.* **2019**, *42*, 167–191. [CrossRef]
3. Tang, Y.B.T.; Panwisawas, C.; Ghoussoub, J.N.; Gong, Y.L.; Clark, J.W.G.; Nemeth, A.A.N.; McCartney, D.G.; Reed, R.C. Alloys-by-design: Application to new superalloys for additive manufacturing. *Acta Mater.* **2021**, *202*, 417–436. [CrossRef]
4. Yang, F.P.; Wen, T.; Zhang, L.; Wang, J.Y.; Huang, S.L.; Ji, S.X.; Yang, H.L. Role of inclination angle on columnar-to-equiaxed transition in the eutectic Al-5Mg-2Si alloy fabricated by laser powder bed fusion. *J. Cent. S. Univ.* **2024**, *3*, 2150–2166. [CrossRef]

5. DebRoy, T.; Wei, H.L.; Zuback, J.S.; Mukherjee, T.; Elmer, J.W.; Milewski, J.O.; Beese, A.M.; Wilson-Heid, A.; De, A.; Zhang, W. Additive manufacturing of metallic components—Process, structure and properties. *Prog. Mater. Sci.* **2018**, *92*, 112–224. [CrossRef]
6. Wang, J.Y.; Zou, J.P.; Yang, H.L.; Liu, Z.L.; Ji, S.X. High strength and ductility of an additively manufactured CrCoNi medium-entropy alloy achieved by minor Mo doping. *Mater. Sci. Eng. A* **2022**, *843*, 143129. [CrossRef]
7. Wang, J.Y.; Yang, H.L.; Liu, Z.L.; Fan, L.; Yan, W.T.; Qiu, D.; Fu, M.W. Compositional regulation in additive manufacturing of precipitation-hardening $(CoCrNi)_{94}Ti_3Al_3$ medium-entropy superalloy: Cellular structure stabilization and strength enhancement. *Compos. Part. B-Eng.* **2024**, *281*, 111570. [CrossRef]
8. Wang, X.; Muniz-Lerma, J.A.; Sanchez-Mata, O.; Shandiz, M.A.; Brodusch, N.; Gauvin, R.; Brochu, M. Characterization of single crystalline austenitic stainless steel thin struts processed by laser powder bed fusion. *Scripta Mater.* **2019**, *163*, 51–56. [CrossRef]
9. Yang, H.L.; Zhang, Y.Y.; Wang, J.Y.; Liu, Z.L.; Liu, C.H.; Ji, S.X. Additive manufacturing of a high strength Al-5Mg_2Si-2Mg alloy: Microstructure and mechanical properties. *J. Mater. Sci. Technol.* **2021**, *91*, 215–223. [CrossRef]
10. Wen, T.; Li, Z.C.; Wang, J.Y.; Luo, Y.M.; Yang, F.P.; Liu, Z.L.; Qiu, D.; Yang, H.L.; Ji, S.X. From crack-prone to crack-free: Eliminating cracks in additive manufacturing of high-strength Mg_2Si-modified Al-Mg-Si alloys. *J. Mater. Sci. Technol.* **2025**, *204*, 276–291. [CrossRef]
11. Ponnusamy, P.; Rashid, R.A.R.; Masood, S.H.; Ruan, D.; Palanisamy, S. Mechanical Properties of SLM-Printed Aluminium Alloys: A Review. *Materials* **2020**, *13*, 4301. [CrossRef]
12. Geng, Y.X.; Wang, Y.M.; Xu, J.H.; Mi, S.B.; Fan, S.M.; Xiao, Y.K.; Wu, Y.; Luan, J.H. A high-strength AlSiMg1.4 alloy fabricated by selective laser melting. *J. Alloys Compd.* **2021**, *867*, 159103. [CrossRef]
13. Yan, Q.; Song, B.; Shi, Y.S. Comparative study of performance comparison of AlSi10Mg alloy prepared by selective laser melting and casting. *J. Mater. Sci. Technol.* **2020**, *41*, 199–208. [CrossRef]
14. Martin, A.; Sebastian, M.S.; Gil, E.; Wang, C.Y.; Milenkovic, S.; Pérez-Prado, M.T.; Cepeda-Jiménez, C.M. Effect of the heat treatment on the microstructure and hardness evolution of a AlSi10MgCu alloy designed for laser powder bed fusion. *Mater. Sci. Eng. A* **2021**, *819*, 141487. [CrossRef]
15. Mei, J.H.; Han, Y.; Sun, J.P.; Zu, G.Q.; Song, X.L.; Zhu, W.W.; Ran, X. Achieving high strength in selective laser melting AlSi10Mg alloy by adding microsized pure Cu particles. *Mater. Sci. Eng. A* **2023**, *880*, 145357. [CrossRef]
16. Kenevisi, M.S.; Yu, Y.F.; Lin, F. A review on additive manufacturing of Al-Cu (2xxx) aluminium alloys, processes and defects. *Mater. Sci. Technol.* **2021**, *37*, 805–829. [CrossRef]
17. Li, X.P.; Ji, G.; Chen, Z.; Addad, A.; Wu, Y.; Wang, H.W.; Vleugels, J.; Van Humbeeck, J.; Kruth, J.P. Selective laser melting of nano-TiB_2 decorated AlSi10Mg alloy with high fracture strength and ductility. *Acta Mater.* **2017**, *129*, 183–193. [CrossRef]
18. Yu, W.H.; Sing, S.L.; Chua, C.K.; Kuo, C.N.; Tian, X.L. Particle-reinforced metal matrix nanocomposites fabricated by selective laser melting: A state of the art review. *Prog. Mater. Sci.* **2019**, *104*, 330–379. [CrossRef]
19. DebRoy, T.; Mukherjee, T.; Wei, H.L.; Elmer, J.W.; Milewski, J.O. Metallurgy, mechanistic models and machine learning in metal printing. *Nat. Rev. Mater.* **2021**, *6*, 48–68. [CrossRef]
20. Han, Q.Q.; Setchi, R.; Lacan, F.; Gu, D.D.; Evans, S.L. Selective laser melting of advanced Al-Al_2O_3 nanocomposites: Simulation, microstructure and mechanical properties. *Mater. Sci. Eng. A* **2017**, *698*, 162–173. [CrossRef]
21. Zhou, Y.; Duan, L.C.; Wen, S.F.; Wei, Q.S.; Shi, Y.S. Enhanced micro-hardness and wear resistance of Al-15Si/TiC fabricated by selective laser melting. *Compos. Commun.* **2018**, *10*, 64–67. [CrossRef]
22. Feng, Z.; Wang, X.M.; Tan, H.; Zhang, F.Y.; Fan, W.; Wang, Y.X.; Fang, Y.B.; Wang, J.L.; Wu, F.; Lin, X.; et al. Effect of heat treatment patterns on porosity, microstructure, and mechanical properties of selective laser melted TiB_2/Al-Si-Mg composite. *Mater. Sci. Eng. A* **2022**, *855*, 143932. [CrossRef]
23. Zhou, S.Y.; Su, Y.; Wang, H.; Enz, J.; Ebel, T.; Yan, M. Selective laser melting additive manufacturing of 7xxx series Al-Zn-Mg-Cu alloy: Cracking elimination by co-incorporation of Si and TiB_2. *Addit. Manuf.* **2020**, *36*, 101458. [CrossRef]
24. Gu, D.D.; Yang, Y.; Xi, L.X.; Yang, J.K.; Xia, M.J. Laser absorption behavior of randomly packed powder-bed during selective laser melting of SiC and TiB_2 reinforced Al matrix composites. *Opt. Laser. Technol.* **2019**, *119*, 105600. [CrossRef]
25. Mair, P.; Kaserer, L.; Braun, J.; Weinberger, N.; Letofsky-Papst, I.; Leichtfried, G. Microstructure and mechanical properties of a TiB_2-modified Al-Cu alloy processed by laser powder-bed fusion. *Mater. Sci. Eng. A* **2021**, *799*, 140209. [CrossRef]
26. Xiao, Y.K.; Chen, H.; Bian, Z.Y.; Sun, T.T.; Ding, H.; Yang, Q.; Wu, Y.; Lian, Q.; Chen, Z.; Wang, H.W. Enhancing strength and ductility of AlSi10Mg fabricated by selective laser melting by TiB_2 nanoparticles. *J. Mater. Sci. Technol.* **2022**, *109*, 254–266. [CrossRef]
27. Jiang, F.Q.; Tang, L.; Li, S.; Ye, H.Q.; Attallah, M.M.; Yang, Z.Q. Achieving strength-ductility balance in a laser powder bed fusion fabricated TiB_2/Al-Cu-Mg-Ag alloy. *J. Alloys Compd.* **2023**, *945*, 169311. [CrossRef]
28. Bi, J.; Lei, Z.L.; Chen, X.; Li, P.; Lu, N.N.; Chen, Y.B. Microstructure and mechanical properties of TiB_2-reinforced 7075 aluminum matrix composites fabricated by laser melting deposition. *Ceram. Int.* **2019**, *45*, 5680–5692.
29. Xi, L.; Wang, P.; Prashanth, K.G.; Li, H.; Prykhodko, H.V.; Scudino, S.; Kaban, I. Effect of TiB_2 particles on microstructure and crystallographic texture of Al-12Si fabricated by selective laser melting. *J. Alloys Compd.* **2019**, *786*, 551–556. [CrossRef]
30. Chen, B.; Xi, X.; Gu, T.; Tan, C.W.; Song, X.G. Influence of heat treatment on microstructure evolution and mechanical properties of TiB_2/Al 2024 composites fabricated by directed energy deposition. *J. Mater. Res. Technol.* **2020**, *9*, 14223–14236. [CrossRef]

31. Geng, Y.X.; Wang, Q.; Wang, Y.M.; Zang, Q.H.; Mi, S.B.; Xu, J.H.; Xiao, Y.K.; Wu, Y.; Luan, J.H. Microstructural evolution and strengthening mechanism of high-strength AlSi8.1Mg1.4 alloy produced by selective laser melting. *Mater. Des.* **2022**, *218*, 110674. [CrossRef]
32. Xiao, Y.K.; Bian, Z.Y.; Wu, Y.; Ji, G.; Li, Y.Q.; Li, M.J.; Lian, Q.; Chen, Z.; Addad, A.; Wang, H.W. Effect of nano-TiB_2 particles on the anisotropy in an AlSi10Mg alloy processed by selective laser melting. *J. Alloys Compd.* **2019**, *798*, 644–655. [CrossRef]
33. Salim, E.T.; Ismail, R.A.; Halbos, H.T. Growth of Nb_2O_5 film using hydrothermal method: Effect of Nb concentration on physical properties. *Mater. Res. Express.* **2019**, *6*, 116429. [CrossRef]
34. Buhairi, M.A.; Foudzi, F.M.; Jamhari, F.I.; Sulong, A.; Radzuan, N.A.M.; Muhamad, N.; Mohamed, I.F.; Azman, A.H.; Harun, W.S.W.; Al-Furjan, M.S.H. Review on volumetric energy density: Influence on morphology and mechanical properties of Ti6Al4V manufactured via laser powder bed fusion. *Prog. Addit. Manuf.* **2023**, *8*, 265–283. [CrossRef]
35. Amirkhanlou, S.; Ji, S.X.; Zhang, Y.J.; Watson, D.; Fan, Z.Y. High modulus Al-Si-Mg-Cu/Mg_2Si-TiB_2 hybrid nanocomposite: Microstructural characteristics and micromechanics-based analysis. *J. Alloys Compd.* **2017**, *694*, 313–324. [CrossRef]
36. Wang, J.Y.; Zou, J.P.; Yang, H.L.; Dong, X.X.; Cao, P.; Liao, X.Z.; Liu, Z.L.; Ji, S.X. Ultrastrong and ductile $(CoCrNi)_{94}Ti_3Al_3$ medium-entropy alloys via introducing multi-scale heterogeneous structures. *J. Mater. Sci. Technol.* **2023**, *135*, 241–249. [CrossRef]
37. Prashanth, K.G.; Eckert, J. Formation of metastable cellular microstructures in selective laser melted alloys. *J. Alloys Compd.* **2017**, *707*, 27–34. [CrossRef]
38. Saboori, A.; Aversa, A.; Marchese, G.; Biamino, S.; Lombardi, M.; Fino, P. Microstructure and Mechanical Properties of AISI 316L Produced by Directed Energy Deposition-Based Additive Manufacturing: A Review. *Appl. Sci.* **2020**, *10*, 3310. [CrossRef]
39. Liu, P.W.; Wang, Z.; Xiao, Y.H.; Horstemeyer, M.F.; Cui, X.Y.; Chen, L. Insight into the mechanisms of columnar to equiaxed grain transition during metallic additive manufacturing. *Addit. Manuf.* **2019**, *26*, 22–29. [CrossRef]
40. Wang, Q.Z.; Lin, X.; Kang, N.; Wen, X.L.; Cao, Y.; Lu, J.L.; Peng, D.J.; Bai, J.; Zhou, Y.X.; El Mansori, M.; et al. Effect of laser additive manufacturing on the microstructure and mechanical properties of TiB_2 reinforced Al-Cu matrix composite. *Mater. Sci. Eng. A* **2022**, *840*, 142950. [CrossRef]
41. Fan, Z.; Wang, Y.; Zhang, Y.; Qin, T.; Zhou, X.R.; Thompson, G.E.; Pennycook, T.; Hashimoto, T. Grain refining mechanism in the Al/Al-Ti-B system. *Acta Mater.* **2015**, *84*, 292–304. [CrossRef]
42. Chen, B.; Moon, S.K.; Yao, X.; Bi, G.; Shen, J.; Umeda, J.; Kondoh, K. Strength and strain hardening of a selective laser melted AlSi10Mg alloy. *Scr. Mater.* **2017**, *141*, 45–49. [CrossRef]
43. Feng, Z.; Tan, H.; Fang, Y.B.; Lin, X.; Huang, W.D. Selective laser melting of TiB_2/AlSi10Mg composite: Processability, microstructure and fracture behavior. *J. Mater. Process. Tech.* **2022**, *299*, 117386. [CrossRef]
44. Chen, Y.; Jian, Z.Y.; Ren, Y.M.; Li, K.; Dang, B.; Guo, L.X. Influence of TiB_2 volume fraction on SiCp/AlSi10Mg composites by PBF-LB: Microstructure, mechanical, and physical properties. *J. Mater. Res. Technol.* **2023**, *233*, 697–3710.
45. Wang, J.Y.; Fang, J.H.; Yang, H.L.; Liu, Z.L.; Li, R.D.; Ji, S.X.; Wang, Y.; Ruan, J.M. Mechanical properties and wear resistance of medium entropy $Fe_{40}Mn_{40}Cr_{10}Co_{10}$/TiC composites. *Trans. Nonferrous Met. Soc. China* **2019**, *29*, 1484–1494. [CrossRef]
46. Wang, J.Y.; Yang, H.L.; Liu, Z.L.; Li, R.D.; Ruan, J.M.; Ji, S.X. Synergistic effects of WC nanoparticles and MC nanoprecipitates on the mechanical and tribological properties of $Fe_{40}Mn_{40}Cr_{10}Co_{10}$ medium-entropy alloy. *J. Mater. Res. Technol.* **2019**, *8*, 3550–3564. [CrossRef]
47. Li, N.; Wang, T.; Zhang, L.X.; Zhang, L. Coupling effects of SiC and TiB_2 particles on crack inhibition in Al-Zn-Mg-Cu alloy produced by laser powder bed fusion. *J. Mater. Sci. Technol.* **2023**, *164*, 37–51. [CrossRef]
48. Li, J.H.; Hage, F.S.; Ramasse, Q.M.; Schumacher, P. The nucleation sequence of α-Al on TiB_2 particles in Al-Cu alloys. *Acta Mater.* **2021**, *206*, 116652. [CrossRef]
49. Cui, Y.; King, D.J.M.; Horsfield, A.P.; Gourlay, C.M. Solidification orientation relationships between Al_3Ti and TiB_2. *Acta Mater.* **2020**, *186*, 149–161. [CrossRef]
50. Mair, P.; Goettgens, V.S.; Rainer, T.; Weinberger, N.; Letofsky-Papst, I.; Mitsche, S.; Leichtfried, G. Laser powder bed fusion of nano-CaB_6 decorated 2024 aluminum alloy. *J. Alloys Compd.* **2021**, *863*, 158714. [CrossRef]
51. Cheng, W.; Liu, Y.Z.; Xiao, X.J.; Huang, B.; Zhou, Z.G.; Liu, X.H. Microstructure and mechanical properties of a novel (TiB_2+TiC)/AlSi10Mg composite prepared by selective laser melting. *Mater. Sci. Eng. A* **2022**, *834*, 142435. [CrossRef]
52. Sun, T.T.; Chen, J.; Wu, Y.; Wang, M.L.; Fu, Y.A.; Wang, H.Z.; Wang, H.W. Achieving excellent strength of the PBF-LB additively manufactured Al-Cu-Mg composite via in-situ mixing TiB_2 and solution treatment. *Mater. Sci. Eng. A* **2022**, *850*, 143531. [CrossRef]
53. Yang, K.V.; Rometsch, P.; Davies, C.H.J.; Huang, A.; Wu, X. Effect of heat treatment on the microstructure and anisotropy in mechanical properties of A357 alloy produced by selective laser melting. *Mater. Des.* **2018**, *154*, 275–290. [CrossRef]